

Cuprate-like Electronic Structures in Infinite-Layer Nickelates with 3D dispersion

X. Ding,^{1,*} Y. Fan,^{1,*} X. X. Wang,¹ C. H. Li,¹ Z. T. An,¹ J. H. Ye,¹ S. L. Tang,¹ M. Y. N. Lei,¹ X. T. Sun,¹ N. Guo,¹ Z. H. Chen,¹ S. Sangphet,¹ Y. L. Wang,^{2,3} H. C. Xu,^{1,4,†} R. Peng,^{1,4,‡} and D. L. Feng^{5,1,3,2,§}

¹*Advanced Materials Laboratory, State Key Laboratory of Surface Physics, and Department of Physics, Fudan University, Shanghai 200433, People's Republic of China*

²*School of Emerging Technology, University of Science and Technology of China, Hefei, 230026, China*

³*New Cornerstone Science Laboratory, University of Science and Technology of China, Hefei, 230026, China*

⁴*Shanghai Research Center for Quantum Sciences, 201315 Shanghai, P. R. China.*

⁵*National Synchrotron Radiation Laboratory and School of Nuclear Science and Technology, University of Science and Technology of China, Hefei, 230026, China*

(Dated: March 13, 2024)

The discovery of superconductivity in the infinite-layer (IL) nickelates¹⁻⁶ provides a new platform and angle of view to study the long-standing problem of high temperature superconductivity⁷⁻¹¹. Many models were proposed to understand its superconducting mechanisms based on the calculated electronic structure, and the multiple Fermi surfaces and multiple orbitals involved create complications and controversial conclusions¹²⁻²⁵. Over the past 5 years, the lack of direct measurements of the electronic structure has hindered the understanding of nickelate superconductors. Here, we fill this gap by preparing IL LaNiO_2 and $\text{La}_{0.8}\text{Ca}_{0.2}\text{NiO}_2$ thin films with superior surface quality and measuring their electronic structure by angle-resolved photoemission spectroscopy (ARPES). The Fermi surface consists of a large three-dimensional hole pocket primarily contributed by Ni- $3d_{x^2-y^2}$ states, and a small electron pocket at the Brillouin zone (BZ) corner. The hole pocket exhibits a two-dimensional character over approximately 80% of the Brillouin zone, and its Fermi surface topology and band dispersion closely resemble those observed in hole-doped cuprates, suggesting their superconducting mechanisms may be alike. Yet this hole pocket shows strong three-dimensional character near $k_z = \pi$, which deviates from previous calculations and adds new facets to the superconductivity in IL nickelates. The experimental electronic structure represents a pivotal step toward a microscopic understanding of the IL nickelate family and its superconductivity.

Introduction

Following the discovery of the high-temperature superconductivity in cuprates²⁶, it was suggested that superconductivity in nickelates could be realized, if the common Ni $3d^8$ could be reduced to $3d^9$ state⁷⁻¹¹. After years of effort, superconductivity was discovered in (Nd,Sr)NiO₂ thin films¹, where the apical oxygens in (Nd,Sr)NiO₃ were removed by reaction with CaH₂ powders. Subsequently, superconductivity was achieved in related compounds such as (La,Sr)NiO₂ (ref.2,3), (La,Ca)NiO₂ (ref.4), (Pr,Sr)NiO₂ (ref.5), (Nd,Eu)NiO₂ (ref.6), *etc.* However, high-quality IL nickelate superconductors are difficult to fabricate²⁷⁻²⁹, and the surface of the IL nickelate superconductors usually becomes disordered in the reduction process^{30,31}, which prevents the reliable measurement of its electronic structure by ARPES or scanning tunneling microscopy (STM).

Various theoretical models on the superconductivity of IL nickelates are based on combinations of different Ni/RE (rare earth) orbitals and Fermi surface topologies. Consequently, distinct superconducting mechanisms could be reached. For instance, Kitatini *et.al.* propose that RENiO_2

can be described by one band Hubbard model with Ni- $3d_{x^2-y^2}$ orbital akin to cuprates, based on which superconducting transition temperature can be estimated¹². However, others suggested that Ni- $3d_{xy}$ or Ni- $3d_{3z^2-r^2}$ orbital and Hund's coupling should be included, potentially yielding a high-spin $S = 1$ state in superconducting nickelates^{13,14}, which might lead to a pairing symmetry distinct from hole-doped cuprates^{15,16}. Additionally, the presence of conduction electrons (including various $RE-d$ orbitals and interstitial s orbitals) and their contributions to superconductivity further complicate the understanding¹⁷⁻²⁴.

Since accurate knowledge of their low-energy electronic structure is critical for modeling the IL nickelates, many fundamental issues need to be pinned down, such as the Fermi surface topology, the orbital characters of bands, the participation of $RE-5d$ or interstitial s orbitals in the low energy electronic structure, *etc.* Particularly, a key question is whether the electronic structure resembles the two-dimensional (2D) Zhang-Rice singlet band in cuprates. However, due to strong electron correlations, an accurate band calculation for IL nickelates is still challenging, thus experimental verification and input are urgently demanded.

Single-crystalline IL surface

Reliable measurements of the electronic structure of IL nickelates require high quality stoichiometric 113 perovskite films, sufficient *in-situ* reduction, and most critically, single-crystalline IL surfaces. A strong reducing condition is required to achieve a topotactic transition to the IL phase, yet a mild reducing condition is needed to avoid damaging the crystalline surface, posing a dilemma. Here we have grown LaNiO_3 and $\text{La}_{0.8}\text{Ca}_{0.2}\text{NiO}_3$ thin films on SrTiO_3 (001) substrates using oxide molecular beam epitaxy with an atomic-layer-by-layer growth method (See Supplementary Section I), and then reduced them *in-situ* with atomic hydrogen. As depicted in Fig. 1a, we have used a shutter to prevent direct H atom bombardment on the sample surface, which effectively avoids disorder formation during the violent topotactic reduction process. In this way, the reflection high energy electron diffraction (RHEED) pattern of the films after the reduction shows sharp streaks from 2D surfaces (Fig. 1a), and atomic force microscopy (AFM) shows terraces with unit-cell step height (Supplementary Fig. S4), indicating single-crystalline and atomically flat sample surfaces. *Ex-situ* X-ray diffraction (XRD) measurements were performed on the same samples after ARPES measurements (Fig. 1b and Fig. S3). The positions of the diffraction peaks are notably shifted to higher values compared to those of the perovskite phase (Fig. 1b), and consistent with the previous report on $(\text{La,Ca})\text{NiO}_2$ (ref.4). The fringes accompanying the diffraction peaks

observed in LaNiO_2 (Supplementary Fig. S3a) and $(\text{La}_{0.8}\text{Ca}_{0.2})\text{NiO}_2$ (Fig. 1b) are comparable to, if not more pronounced than, the previous reports^{2-4,31}, further indicating the high quality of the IL films. The conversion efficiency from perovskite to IL phase is among the highest as compared to literature³¹ (Supplementary Section III). All these results demonstrate the acquisition of the IL phase with superior surface quality.

Following the optimized growth and *in-situ* reduction procedure, 21 unit cell (uc) LaNiO_2 and 25 uc $\text{La}_{0.8}\text{Ca}_{0.2}\text{NiO}_2$ thin films have been prepared for ARPES studies (additional characterizations are provided in Supplementary Section III). Although the $(\text{La,Ca})\text{NiO}_2$ studied here does not exhibit superconductivity down to 2 K, possibly due to the presence of defects, its doping levels correspond to the weakly-insulating and superconducting regimes, respectively, as indicated by the reported phase diagram of $(\text{La,Ca})\text{NiO}_2$ (Fig. 1c, ref. 4). ARPES measurements on these samples show clear band dispersions.

In-plane electronic structure

In-situ ARPES measurements were performed with vacuum ultra-violet (VUV) photons at 15 K on 21 uc thick LaNiO_2 and 25 uc thick $\text{La}_{0.8}\text{Ca}_{0.2}\text{NiO}_2$ films. Remarkably, as shown in Figs. 1d-1e, a large rounded rectangular pocket (red lines, denoted as α) and a small round pocket (blue lines, denoted as β) can be observed around (π, π) in $\text{LaNiO}_2/\text{SrTiO}_3$. With 20% Ca doping that introduces holes, the α pocket expands and the β pocket shrinks (Fig. 1e and Supplementary Section IV).

Figure 2 shows the detailed electronic structure of LaNiO_2 measured by VUV-ARPES. The α band resembles the low-energy Zhang-Rice singlet of cuprates in terms of both Fermi surface shape and band dispersion³². It forms a large rounded square pocket centered at (π, π) (Fig. 2a). Note that the spectral weight intensity is higher in the second Brillouin zone (BZ) (Figs. 1d, 1e, 2a), a phenomenon commonly observed in ARPES studies of cuprates and consistent with the photoemission matrix-element of $3d_{x^2-y^2}$ orbitals. The dispersion of α band exhibits a shallow electron-like dispersion along cut #1 in Figs. 2b and 2c. Along cut #2, the α band's dispersion is steep near the zone center (Fig. 2e) and flattens towards lower binding energy near $(0, \pi)$ (Fig. 2d). These demonstrate a saddle-point dispersion in the $(0, \pi)$ region (Fig. 2f), similar to the dispersion in the anti-nodal region of cuprates³². On the other hand, there is an electron-like band centered at (π, π) (Figs. 2g-2h), which is absent in cuprates. We note that the quasiparticle weight is quite weak, which could be suppressed by the matrix element effects and defects in the samples, and incoher-

ent spectral weight dominates the α band. The incoherent part is commonly observed to follow the calculated bare band, similar to the steep “water-fall” dispersion observed in the cuprates³³.

Three-dimensional electronic structure

To check whether the observed band structure includes any surface state, which might originate from the polar surface of LaNiO_2 , we conducted additional investigations into its three-dimensional electronic structure using soft X-ray ARPES (SX-ARPES) measurements, which offer bulk sensitivity and much higher k_z resolution than VUV-ARPES^{36,37}. To take further precautions, we have prepared 1.2 uc BaTiO_3 (BTO) capped $\text{LaNiO}_2/\text{SrTiO}_3$, as the capping layer was suggested to provide additional protection to the IL surface during reduction³¹, and SX-ARPES can detect the band structure beneath the capping layer³⁵. As shown in Fig. 3b, obvious k_z dispersion is observed in the measurements performed with photon energies ranging from 385 eV to 610 eV around $E_F - 1$ eV. More specifically, the strong photoemission intensity around the Z point in Fig. 3b corresponds to the γ band in Figs. 3c-3d. Some weak features around A near E_F (Fig. 3d) is contributed by the β band (Fig. 2g). Other features in Fig. 3b include the η and ε bands, which approach closely in the Z plane, and separate the most in the Γ plane (Fig. 3e). Such modulation as a function of k_z has the same periodicity as the BZ of LaNiO_2 . These results indicate that all the measured band structure represents the bulk band structure of IL nickelates. It should be noted that the dispersion of bands below and near E_F is consistent in both VUV- and SX-ARPES measurements, regardless of the capping layer (see details in Supplementary Sections V). This consistency suggests that the VUV-ARPES data can also reflect the bulk electronic structure.

Now we examine the low-energy electronic structure at the Z-A-R plane using 253 eV soft X-ray photons, which gives a decent balance between k_z resolution and energy/momentum resolution. There is a small pocket centered at A in the photoemission intensity map (Fig. 4a), whose size matches the β pocket observed in VUV-ARPES (Supplementary Fig. S9). At first glance, the large pocket formed by α seems absent (Fig. 4a). However, upon closer inspection of the dispersion, the α band can be observed at $E - E_F < -0.3$ eV, while near E_F it is buried by the stronger intensity of the β band. As shown in Fig. 4b, the band velocity of the sharp dispersive feature near the A point exhibits a slope sign change around $E_F - 0.3$ eV (Figs. 4b-4c). Specifically, the dispersive feature is dominated by an electron-like dispersion at $E - E_F > -0.3$ eV, and by a hole-like dispersion at $E - E_F < -0.3$ eV, while details of their hybridization cannot be resolved under the current energy resolution. The electron-like dispersion matches the β band observed in the VUV-ARPES

(Supplementary Fig. S9). Away from the Z-A-R plane, the β pocket quickly shrinks (Fig. 4g), forming a rounded square pocket centered at the A point in the Γ -M-A-Z plane, following the period of IL BZ (Fig. 4e).

Using linear-horizontal polarized photons, the intensity of the electron-like dispersion of β band is suppressed. Such polarization dependence is different from the matrix element of $d_{x^2-y^2}$ orbital, but is expected for that of d_{xy} orbital³⁸, consistent with the theoretical calculations suggesting La $5d_{xy}$ show up near the A point³⁹. The suppression of the β band allows the full dispersion of the hole-like dispersion to be resolved. The Fermi momentum of the hole-like dispersion is evidently positioned very close to the A point (Fig. 4d), forming a small hole pocket. Figure 4f shows its k_z -dependent behavior at $E_F - 0.4$ eV, where the dispersive feature is dominated by the hole-like dispersion. As the k_z deviates from the Z-A-R plane, the hole-like dispersion quickly expands (Figs. 4f-4g). It forms a large hole pocket (Figs. 4e) that matches the α pocket observed in VUV-ARPES off the Z plane (Fig. 2a and Supplementary Fig. S10). Notably, the Fermi momentum of the α pocket along the $(0,0)-(\pi,\pi)$ direction has little variation over a large k_z span (Figs. 4e, more data provided in Supplementary Fig. S10). These results consistently suggest that the α band is quasi-two-dimensional off the Z plane and strongly three-dimensional near Z plane.

Comparison with DFT calculations

Figure 5 summarizes the observed band structure and compares it to the DFT calculations. The measured valence band features can be qualitatively matched to the calculated results by DFT. Along Γ -M with $k_z = 0$, the η and ε bands roughly follows the calculated bands with Ni- $3d_{xy}$ and Ni- $3d_{xz}/d_{yz}$ characters, respectively (Figs. 5a and 5f). Along Z-A with $k_z = \pi$, the η and ε bands become closer to each other, while the γ band emerges and matches the Ni- $3d_{3z^2-r^2}$ character in the DFT calculation (Figs. 5b and 5g). Near the Fermi energy, the α band is resolved along Γ -M and matches the Ni- $3d_{x^2-y^2}$ character (Figs. 5a and 5f). The α Fermi surface in the Γ -M-X plane is a large hole pocket centered at M (Fig. 5c), consistent with the calculations (Fig. 5h). As summarized in Fig. 5e, the α band exhibits quasi-2D characteristics, showing minimal variation along k_z in approximately 80% of the BZ. Its Fermi surface and dispersion are similar to the Zhang-Rice singlet observed in cuprates. Along Z-A, the β band is slightly shallower than the calculated electron-like band (Figs. 5b and 5g), which primarily consists of mixed Ni- $3d_{xz/yz}$, La- $5d_{xy}$ and interstitial- s character (ref. 39–41, and Supplementary Fig. S12). The β electron Fermi pocket

at A (Figs. 5d-5e) agrees qualitatively with the calculations (Figs. 5i-5j) aside from its slightly smaller size.

Clear discrepancies can also be observed between the experimental and calculated electronic structures. Compared with the calculated band with Ni- $3d_{x^2-y^2}$ character, the α band shows strikingly strong k_z dispersion in the vicinity of the Z-A-R plane ($k_z = \pi$), and its Fermi crossing is much closer to the A point (Fig. 5b). The tiny α hole pocket at A (Fig. 5d) dramatically differs from the calculated large square electron pocket centered at Z (Fig. 5i). Since the dispersion of the α band follows the calculation at the Γ -X-M plane (Fig. 5a), but differs from that at the Z-A-R plane (Fig. 5b), this difference cannot be explained by a simple chemical potential shift. The strong k_z dispersion of the α band near the Z-A-R plane suggests that its constituents are more than just the Ni- $3d_{x^2-y^2}$ orbitals. Specifically, at $k_z \sim 0.8\pi$ where the α band deviates from quasi-2D behavior, the pocket of the β band appears, suggesting possible interactions between the two bands, especially near the Z plane. Recently, it has been pointed out that substantial hybridization occurs between the Ni- $3d_{x^2-y^2}$ orbital and other orbitals mediated by in-plane oxygens⁴¹. The hybridization is particularly strong with the interstitial s -like orbital occupying the position of the apical oxygen in LaNiO₃ that was removed during the H-reduction, then with the next-nearest-neighbor RE - d_{xy} and RE - $d_{3z^2-r^2}$ orbitals⁴¹. Some suggest that the interstitial s orbital couples with the Ni- $3d_{3z^2-r^2}$ orbitals²⁵. This is supported by the Ni-L₃-edge XAS measurement that indicates the presence of out-of-plane components in Ni- $3d$ holes^{25,42}. Therefore, besides the Ni- $3d_{x^2-y^2}$ orbital, the α band may also contain contributions from interstitial s -orbital, the Ni- $3d_{3z^2-r^2}$, and some RE orbitals, particularly near the Z plane.

The β band was shown to largely consist of RE $3d_{xy}$ orbitals and interstitial orbitals (ref. 41 and Supplementary Fig. S12). However, the possible interactions between the α and β bands may lead to the participation of other orbitals in the β band as well. Furthermore, in DFT calculations, there is an electron pocket at Γ with dominant La- $5d_{3z^2-r^2}$ character, but it is not observed in our experiment (Supplementary Fig. S11), which might relate to correlation effects or orbital mixing that could change the dispersion. These observations suggest that the self-doping effect is weaker than what the calculations predicted. All these discrepancies call for more accurate considerations of correlation effects and band calculations.

Discussion and Outlook

Fermi surface volume can be calculated by taking the k_z dispersion of the pockets into account

(see detailed calculations in Supplementary Section IX), which gives the estimated 0.99 ± 0.05 holes in the α pocket and 0.035 electrons in the β pockets for LaNiO_2 . For $\text{La}_{0.8}\text{Ca}_{0.2}\text{NiO}_2$, assuming it has the same k_z dispersion as LaNiO_2 , one can roughly estimate 1.19 ± 0.05 holes in the α pocket and 0.025 electrons in the β pockets (Supplementary Section IX). The net carriers in one unit cell are 0.96 ± 0.05 holes and 1.17 ± 0.05 holes for LaNiO_2 and $\text{La}_{0.8}\text{Ca}_{0.2}\text{NiO}_2$, respectively, roughly matching their chemical formulae. This indicates that Ca could effectively alter the Fermi surface and hole doping, and the band structures and Fermi surfaces found here represent those of the optimally doped IL nickelate and its parent compound.

The α band is largely k_z -independent over 80% of the BZ, exhibiting cuprate-like Fermi surfaces. If we consider this portion as the Fermi surface of a 2D system, this hypothetical 2D system would have 1.11 holes and 1.34 holes for the LaNiO_2 and $\text{La}_{0.8}\text{Ca}_{0.2}\text{NiO}_2$ Fermi surfaces, respectively. The significantly higher hole doping at the 2D part of α indicates a transfer of holes from regions near the Z plane to the 2D part. This uneven distribution of electrons/holes over the momentum space makes the undoped LaNiO_2 far from the half-doped Mott insulator. More remarkably, despite of resemblance, the 2D part of the α band in optimally doped $\text{La}_{0.8}\text{Ca}_{0.2}\text{NiO}_2$, possesses an ultra-high doping level of 34%, placing it in the over-doped and non-superconducting regime of the cuprates⁴³. These findings highlight the intriguing differences between the nickelate and cuprate superconductors.

Charge order was reported in RENiO_2 by resonant X-ray scattering⁴⁴⁻⁴⁶. However, it was recently shown that it may be the structural order of oxygen vacancies⁴⁷. Our results show that the α Fermi surface contains large parallel sectors, but the nesting vector is about $q = (0.23, 0)$ in reciprocal lattice unit, very different from the charge order wavevectors in scattering experiments^{44-46,48}. Therefore, the observed charge order in LaNiO_2 is unlikely to originate from Fermi surface nesting.

To summarize, by improving the surface quality, we experimentally revealed the low-energy electronic structure of IL nickelates. Our ARPES measurements have revealed a large hole pocket α that bears resemblance to the Zhang-Rice singlet Fermi surface in cuprates and is effectively hole-doped under Ca doping. The pronounced three-dimensional behavior near $k_z = \pi$, together with weak but finite self-doping effect, differs from the electronic structure of cuprates, and posing constraints to theories. These findings clarified the fundamental issues on the electronic structure of IL nickelates, which paves the way toward the understanding of the superconductivity mechanism in IL nickelates. The method developed for obtaining the single-crystalline surface of

IL nickelates also opens avenues for further surface-sensitive experimental studies on this family of compounds.

Methods

Thin films growth. Perovskite (La,Ca)NiO₃ thin films were grown on TiO₂-terminated SrTiO₃ (001) substrates by oxide molecular beam epitaxy. A layer-by-layer growth mode is used, in which the A site element (La, Ca) and B site element (Ni) were deposited alternatively, while La and Ca were co-deposited to get uniform doping. The flux of each element were measured by quartz crystal microbalance (QCM), and then calibrated by Rutherford backscattering spectrometry (RBS) measurements. X-ray reflection (XRR) measurements were performed to further calibrate the absolute thickness of the films. XRD measurements were performed to optimize the growth conditions. After optimization, LaNiO₃ and Ca-doped LaNiO₃ were grown at 580 °C under an ozone pressure of 5×10^{-6} mbar and 1.5×10^{-5} mbar, respectively. The 2D character of RHEED pattern is maintained during growth, indicating the single-crystalline and two dimensional sample surface. The doping level calibrated by Rutherford backscattering spectrometry is then further checked by X-ray photoemission on the samples after ARPES studies. More details on growth can be found in Supplementary Section I.

***In-situ* reduction.** After growth, the precursor thin films were transferred *in-situ* to the pulsed laser deposition (PLD) chamber for reduction. Our PLD system is integrated with an atomic hydrogen gun, which generates atomic hydrogen by dissociating H₂ gas through plasma. IL LaNiO₂ (La_{0.8}Ca_{0.2}NiO₂) thin films were obtained by annealing perovskite precursors in an atomic hydrogen environment for 1 (2) hours at 340°C, with a ramp rate of 15 °C/min. During the reduction process, the H₂ gas flow rate was fixed at 3 sccm, and the chamber pressure was around 1.0×10^{-5} mbar. A metal shutter was used to prevent surface crystal structure degradation caused by exposure to H⁺ (Fig. 1a). Under the optimized conditions, perovskite nickelates were transformed into IL nickelates, as confirmed by the X-ray diffraction pattern (see Fig. 1b and Fig S3a). Meanwhile, the fully-strained feature (Fig. S3b) and the terraced surfaces were maintained in IL samples (Fig. S4). Further details on the reduction process and its optimization can be found in Supplementary Sections II and III.

ARPES measurements. All the ARPES experiments were performed at the Shanghai Syn-

chrotron Radiation Facility (SSRF). All samples were reduced *in-situ* and then transferred to beamline by vacuum suitcases and measured under an ultra-high vacuum better than 7×10^{-11} mbar. The SX-ARPES data and the complementary VUV-ARPES data were collected at beamline 09U and beamline 03U, respectively. In VUV ARPES experiments, we set the energy resolution power to 3000 for higher photon flux, which gives a typical energy resolution of 40 meV at 145eV photon energy. The estimated energy resolution of SX-ARPES is 240 meV at 250 eV, and 350 meV at 400 eV. The angle resolution is 0.1° .

DFT calculations. The DFT calculations are performed using the VASP package^{49,50}, with exchange-correlation functional of generalized gradient approximation (GGA)⁵¹. The experimental lattice parameters, $a=b=3.905 \text{ \AA}$ and $c = 3.393 \text{ \AA}$ are used. The energy cutoff of the plane-wave basis is set to be 500 eV. Γ -centered $11 \times 11 \times 11$ and $41 \times 41 \times 41$ K-point grids are used for the charge self-consistent and Fermi surface calculations, respectively. A tight-binding (TB) Hamiltonian, consisting of La-5*d*, La-4*f*, Ni-3*d*, O-2*p* and the interstitial *s* orbital that is centered on (0,0,0.5), is constructed using the Wannier90 package⁵². The band characters are then analyzed in terms of these Wannier orbitals.

Acknowledgement

We gratefully acknowledge the valuable discussion with Prof. Guangming Zhang, Prof. Jiangping Hu, and Prof. Hanghui Chen on theories, and Prof. Liang Qiao, Prof. Tong Zhang, Prof. Juan Jiang, and Ms. Yan Zhao on experiments. We thank Dr. Zhengtai Liu and Dr. Zhenhua Chen for the experimental support during the beamtime. We thank Prof. Liang Qiao, Prof. Yanwu Xie, Prof. Zhaoliang Liao, and Prof. Lingfei Wang, for providing samples grown by PLD in the early stage of this project. We thank Dr. Qingqin Ge for the XPS measurement. This work is supported in part by the National Science Foundation of China under the grant Nos. 12074074, 12274085, 12174365, the National Key R&D Program of the MOST of China (2023YFA1406300), the New Cornerstone Science Foundation, the Innovation Program for Quantum Science and Technology (Grant No. 2021ZD0302803), and Shanghai Municipal Science and Technology Major Project (Grant No.2019SHZDZX01). Part of this research used Beamline 03U of the Shanghai Synchrotron Radiation Facility, which is supported by ME2 project under contract no. 11227902 from National Natural Science Foundation of China.

Author contributions

R.P., H.C.X., Y.F., Z.T.A., J.H.Y., S.L.T., and Z.H.C grew the perovskite films. X.D. and C.H.L.

performed in-situ reduction and surface optimization. X.D., X.X.W., and C.H.L. set up the atomic hydrogen source. X.D., Z.T.A., J.H.Y., S.L.T., and S.S. performed various characterizations on the thin films. X.X.W., X.T.S., and N.G. are in charge of the maintenance of the oxide MBE system. R.P., H.C.X., X.D., X.X.W., J.H.Y., M.Y.N.L., Y.F., C.H.L., and Z.H.C. performed ARPES measurements. R.P., H.C.X., and X.D. analyzed the ARPES data. Y.L.W. conducted the DFT calculations. D.L.F., R.P., and H.C.X. wrote the paper. D.L.F., R.P., and H.C.X. are responsible for the infrastructure, project direction, and planning.

Additional Information

The authors declare no competing interests. Correspondence and requests for materials should be addressed to H. C. Xu, R. Peng or D. L. Feng..

* These authors contributed equally to this work.

† Electronic address: xuhaichao@fudan.edu.cn

‡ Electronic address: pengrui@fudan.edu.cn

§ Electronic address: dlffeng@ustc.edu.cn

¹ Li, D. et al. Superconductivity in an infinite-layer nickelate. *Nature* **572**, 624-627 (2019).

² Osada, M. et al. Nickelate superconductivity without rare-earth magnetism: (La,Sr)NiO₂. *Adv. Mater.* **33**, 2104083 (2021).

³ Sun, W. et al. Evidence for anisotropic superconductivity beyond Pauli limit in infinite-layer lanthanum nickelates. *Adv. Mater.* **35**, 2303400 (2023).

⁴ Zeng, S. et al. Superconductivity in infinite-layer nickelate La_{1-x}Ca_xNiO₂ thin films. *Sci. Adv.* **8**, eabl9927 (2022).

⁵ Osada, M. et al. A Superconducting praseodymium nickelate with infinite layer structure. *Nano Lett.* **20**, 5735-5740 (2020).

⁶ Wei, W. et al. Superconducting Nd_{1-x}Eu_xNiO₂ thin films using in situ synthesis. *Sci. Adv.* **9**, eadh3327 (2023).

⁷ Anisimov, V. I., Bukhvalov, D. & Rice, T. M. Electronic structure of possible nickelate analogs to the cuprates. *Phys. Rev. B* **59**, 7901-7906 (1999).

⁸ Lee, K.-W. & Pickett, W. E. Infinite-layer LaNiO₂: Ni¹⁺ is not Cu²⁺. *Phys. Rev. B* **70**, 165109 (2004).

⁹ Chaloupka, J. & Khaliullin, G. Orbital order and possible superconductivity in LaNiO₃/LaMO₃ super-

- lattices. *Phys. Rev. Lett.* **100**, 016404 (2008).
- ¹⁰ Hansmann, P. et al. Turning a nickelate Fermi surface into a cuprate-like one through heterostructuring. *Phys. Rev. Lett.* **103**, 016401 (2009).
- ¹¹ Han, M. J. et al. Dynamical mean-field theory of nickelate superlattices. *Phys. Rev. Lett.* **107**, 206804 (2011); erratum **110**, 179904 (2013).
- ¹² Kitatani, Motoharu, Liang Si, Oleg Janson, Ryotaro Arita, Zhicheng Zhong, and Karsten Held. Nickelate superconductors—a renaissance of the one-band Hubbard model. *npj Quant. Mater.* **5**, 59 (2020).
- ¹³ Jiang, M., Berciu, M. & Sawatzky, G. A. Critical Nature of the Ni Spin State in Doped NdNiO₂. *Phys. Rev. Lett.* **124**, 207004 (2020).
- ¹⁴ Zhang, Y.-H. & Vishwanath, A. Type-II t-J model in superconducting nickelate Nd_{1-x}Sr_xNiO₂. *Phys. Rev. Res.* **2**, 023112 (2020).
- ¹⁵ Hu, L. and Wu C. Two-band model for magnetism and superconductivity in nickelates. *Phys. Rev. Res.* **1**, 032046 (2019).
- ¹⁶ Werner, Philipp, and Shintaro Hoshino. Nickelate superconductors: Multiorbital nature and spin freezing. *Phys. Rev. B* **101**, 041104 (2020).
- ¹⁷ Hepting, M. et al. Electronic structure of the parent compound of superconducting infinite-layer nickelates. *Nat. Mater.* **19**, 381-385 (2020).
- ¹⁸ Wu, X. et al. Robust d_{x²-y²}-wave superconductivity of infinite-layer nickelates. *Phys. Rev. B* **101**, 060504 (2020).
- ¹⁹ Nomura, Y. et al. Formation of a two-dimensional single-component correlated electron system and band engineering in the nickelate superconductor NdNiO₂. *Phys. Rev. B* **100**, 205138 (2019).
- ²⁰ Gao, J. et al. Electronic structures and topological properties in nickelates Ln_{n+1}Ni_nO_{2n+2}. *Natl. Sci. Rev.* **8**, nwaa218 (2021).
- ²¹ Jiang, P., Si, L., Liao, Z. & Zhong, Z. Electronic structure of rare-earth infinite-layer RNiO₂ (R=La, Nd). *Phys. Rev. B* **100**, 201106 (2019).
- ²² Botana, A. S., & M. R Norman. Similarities and Differences between LaNiO₂ and CaCuO₂ and Implications for Superconductivity. *Phys. Rev. X* **10**, 011024 (2020).
- ²³ Lechermann, F. Late transition metal oxides with infinite-layer structure: Nickelates versus cuprates. *Phys. Rev. B* **101**, 081110 (2020).
- ²⁴ Karp, J. et al. Many-Body Electronic Structure of NdNiO₂ and CaCuO₂. *Phys. Rev. X* **10**, 021061 (2020).

b

- ²⁵ Foyevtsova, K., Elfimov, I., & Sawatzky, G. A. Distinct electridelike nature of infinite-layer nickelates and the resulting theoretical challenges to calculate their electronic structure. *Phys. Rev. B* **108**, 205124 (2023).
- ²⁶ Bednorz, J. G. & Müller, K. A. Possible high T_c superconductivity in the Ba-La-Cu-O system. *Z. Phys. B* **64**, 189-193 (1986).
- ²⁷ Lee, K. et al. Aspects of the synthesis of thin film superconducting infinite-layer nickelates, *APL Mater.* **8**, 041107 (2020).
- ²⁸ Gao, Q., Zhao, Y., Zhou, X., & Zhu, Z. Preparation of superconducting thin films of infinite-layer nickelate $\text{Nd}_{0.8}\text{Sr}_{0.2}\text{NiO}_2$. *Chin. Phys. Lett.* **38**, 077401 (2021).
- ²⁹ Osada, M. et al. Improvement of superconducting properties in $\text{La}_{1-x}\text{Sr}_x\text{NiO}_2$ thin films by tuning topochemical reduction temperature. *Phys. Rev. Mater.* **7**, L051801 (2023).
- ³⁰ Chow, L. E. & Ariando, A. Infinite-layer nickelate superconductors: A current experimental perspective of the crystal and electronic structures. *Front. Phys.* **10**, 834658 (2022).
- ³¹ Parzyck, C. T. et al. Synthesis of thin film infinite-layer nickelates by atomic hydrogen reduction: clarifying the role of the capping layer. Preprint at <https://arxiv.org/abs/2401.07129v1> (2024)
- ³² Andrea D. et al. Angle-resolved photoemission studies of the cuprate superconductors. *Rev. Mod. Phys.* **75**, 473-539 (2003).
- ³³ Xie, B. P. et al. High-energy scale revival and giant kink in the dispersion of a cuprate superconductor. *Phys. Rev. Lett.* **98**, 147001 (2007).
- ³⁴ Rath, M. et al. Scanning tunnelling microscopy and X-ray photoemission studies of NdNiO_2 infinite-layer nickelates films. Preprint at <https://arxiv.org/abs/2402.03143>(2023).
- ³⁵ Chen, X. et al. Orientation-dependent electron-phonon coupling in interfacial superconductors $\text{LaAlO}_3/\text{KTaO}_3$. Preprint at <https://arxiv.org/abs/2301.13488>(2023)
- ³⁶ Strocov, V. N. et al. Soft-x-ray ARPES facility at the ADDRESS beamline of the SLS: concepts, technical realisation and scientific applications. *J. Synchrotron. Rad.* **21**, 32-44 (2014).
- ³⁷ Strocov, V. N. et al. High-resolution soft x-ray beamline ADDRESS at the Swiss Light Source for resonant inelastic x-ray scattering and angle-resolved photoelectron spectroscopies. *J. Synchrotron. Rad.* **17**, 631-43 (2010).
- ³⁸ Zhang, Y. et al. Orbital characters of bands in the iron-based superconductor $\text{BaFe}_{1.85}\text{Co}_{0.15}\text{As}_2$. *Phys. Rev. B* **83**, 054510 (2011).
- ³⁹ Sakakibara, H. et al. Model construction and a possibility of cupratelike pairing in a new d^9 nickelate

- superconductor (Nd,Sr)NiO₂. *Phys. Rev. Lett.* **125**(7), 077003 (2020).
- ⁴⁰ Been, E. et al. Electronic structure trends across the rare-earth series in superconducting infinite-layer nickelates. *Phys. Rev. X* **11**, 011050 (2021).
- ⁴¹ Gu, Y. et al. A substantial hybridization between correlated Ni-d orbital and itinerant electrons in infinite-layer nickelates. *Commun. Phys.* **3**, 84 (2020).
- ⁴² Rossi, M. et al. Orbital and spin character of doped carriers in infinite-layer nickelates. *Phys. Rev. B* **104**, L220505 (2021).
- ⁴³ Rossi, M. et al. From quantum matter to high-temperature superconductivity in copper oxides. *Nature* **518**, 179-186 (2015)
- ⁴⁴ Rossi, M. et al. A broken translational symmetry state in an infinite-layer nickelate. *Nat. Phys.* **18**, 869–873 (2022)
- ⁴⁵ Krieger, G. et al. Charge and spin order dichotomy in NdNiO₂ driven by the capping Layer. *Phys. Rev. Lett.* **129**, 027002 (2022)
- ⁴⁶ Tam, C. C. et al. Charge density waves in infinite-layer NdNiO₂ nickelates. *Nat. Mater.* **615**, 50-55 (2022).
- ⁴⁷ Parzyck, C. T. et al. Absence of $3a_0$ charge density wave order in the infinite-layer nickelate NdNiO₂. *Nat. Mater.* , (2024).
- ⁴⁸ Rossi, M. et al. Universal orbital and magnetic structures in infinite-layer nickelates. Preprint at <https://arxiv.org/abs/2312.16444>. (2023)
- ⁴⁹ Blöchl, P. E. Efficient iterative schemes for *ab initio* total-energy calculations using a plane-wave basis set. *Phys. Rev. B* **54**, 11169 (1996).
- ⁵⁰ Kresse, G. & Furthmüller, J. Projector augmented-wave method. *Phys. Rev. B* **50**, 17953 (1994).
- ⁵¹ Perdew, J. P. et al. Generalized gradient approximation made simple. *Phys. Rev. Lett.* **77**, 3865 (1996).
- ⁵² Mostofi, A. A. An updated version of wannier90: A tool for obtaining maximally-localised Wannier functions. *Comput. Phys. Commun.* **185**, 2309 (2014)

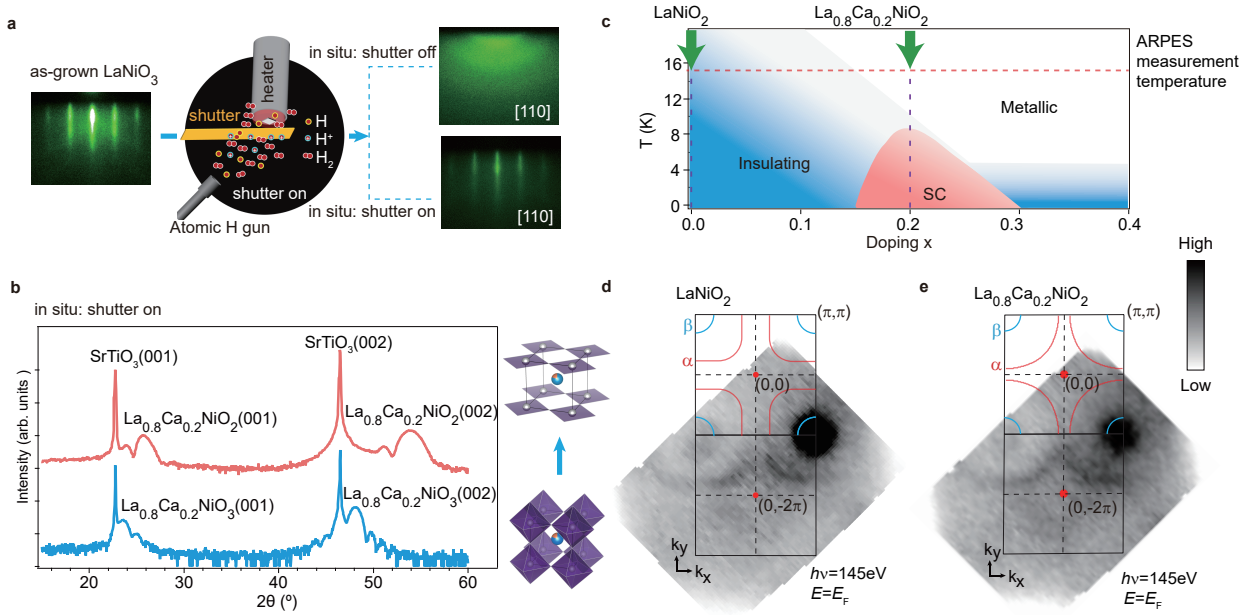


FIG. 1: *In-situ* reduction and optimization to get atomically flat and clean surfaces for ARPES measurements. **a**, Evolution of RHEED image along the [110] azimuth after *in-situ* reduction. The RHEED pattern is single-crystalline (poly-crystalline) when the shutter is on (off) during reduction. The shutter was designed to screen the by-product H^+ generated with atomic H. **b**, The XRD θ - 2θ scans of the perovskite 25 uc $La_{0.8}Ca_{0.2}NiO_3/SrTiO_3$ and *in-situ* reduced IL $La_{0.8}Ca_{0.2}NiO_2/SrTiO_3$. **c**, The doping levels of our samples for ARPES measurements are illustrated in the phase diagram of $(La,Ca)NiO_2$ adapted from Ref.4. ARPES measurements were all performed at 15 K. **d**, **e**, Photoemission intensity map of 21 uc $LaNiO_2/SrTiO_3$ and 25 uc $La_{0.8}Ca_{0.2}NiO_2/SrTiO_3$ at E_F taken with 145 eV photons. The integration is over the energy window of $E_F \pm 0.1$ eV. The red rounded rectangular pocket and blue small pocket are denoted as α and β pockets, respectively. Due to the poor k_z resolution in VUV-ARPES, the data are plotted on a 2D projected Brillouin zone (BZ). The position of k_z is slightly off the Z-plane (see the 145 eV cut in Fig. 4e), and thus both β pocket and the 2D part of the α pocket in 2nd BZ can be observed. k_x and k_y correspond to the two perpendicular Ni-O-Ni directions.

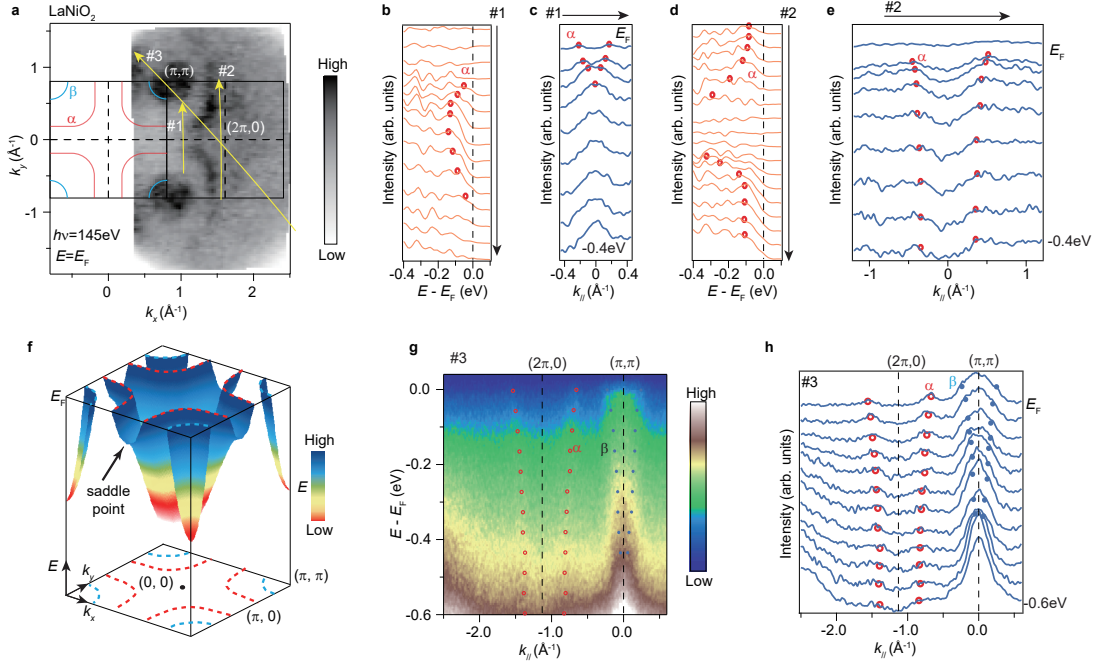


FIG. 2: Cuprate-like low-energy electronic structure of LaNiO₂. **a**, Photoemission intensity map of 21 μ c LaNiO₂/SrTiO₃ at E_F taken with 145 eV photons. The integration is over the energy window of $E_F \pm 0.1$ eV. The Fermi surfaces of a cuprate-like hole pocket α and an electron pocket β are illustrated. **b**, Energy distribution curves (EDCs) along the momentum cut #1. **c**, Momentum distribution curves (MDCs) along the momentum cut #1. **d**, the same as panel **b**, but along cut #2. **e** the same as panel **c**, but along cut #2. **f**, Schematic dispersion of α and β band. The saddle point of α band is indicated. **g**, Photoemission intensity along cut #3. **h**, MDCs along cut #3. The circle markers track the local maxima/shoulders to demonstrate the dispersion of α band (red circles) β band (blue circles).

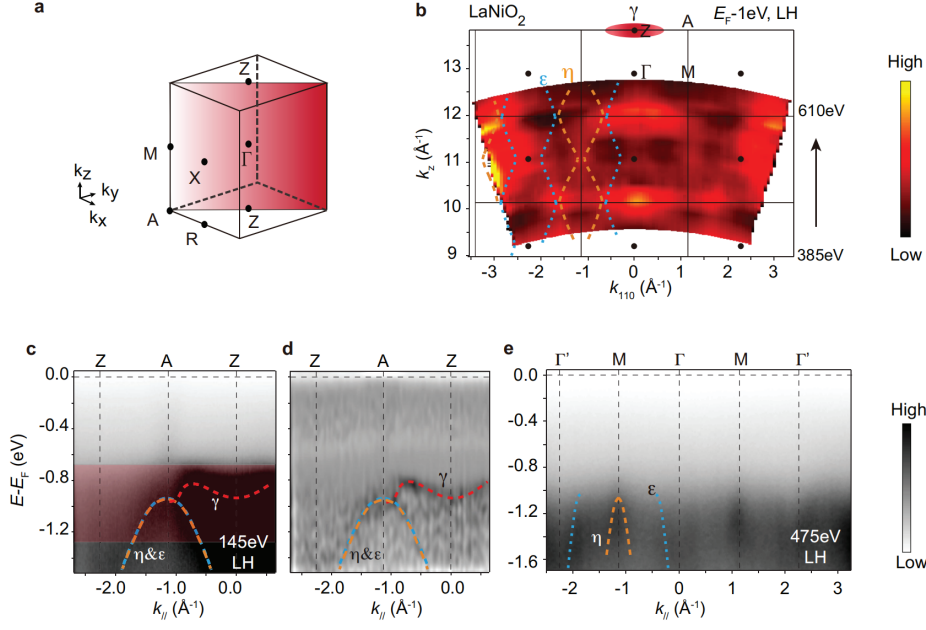


FIG. 3: Three-dimensional valence band dispersion of the IL structure. **a**, Sketch of the Γ -M-A-Z plane where k_z dependent measurements were conducted. **b**, k_z dependent photoemission intensity of 1.2uc-BTO/21uc-LaNiO₂/SrTiO₃ integrated around $E_F - 1$ eV taken with photons from 385 eV to 610 eV in linear horizontal (LH) polarization. The integration window is illustrated by the red-shaded region in panel **c**. The dispersive features are determined by MDCs (Supplementary Fig.S10) and highlighted at the left part by dashed curves (the ε and η bands) and orange patches (γ band), whose period along k_z matches the BZ of IL nickelate structure. **c,d**, Photoemission intensity (**c**) and its 2D curvature (**d**) along Z-A-Z measured on 21uc-LaNiO₂/SrTiO₃. The dispersion of the γ and η bands are illustrated according to the curvature minima. **e**, Photoemission intensity along M- Γ -M measured on 1.2uc-BTO/21uc-LaNiO₂/SrTiO₃, where the dispersion of ε band is resolved.

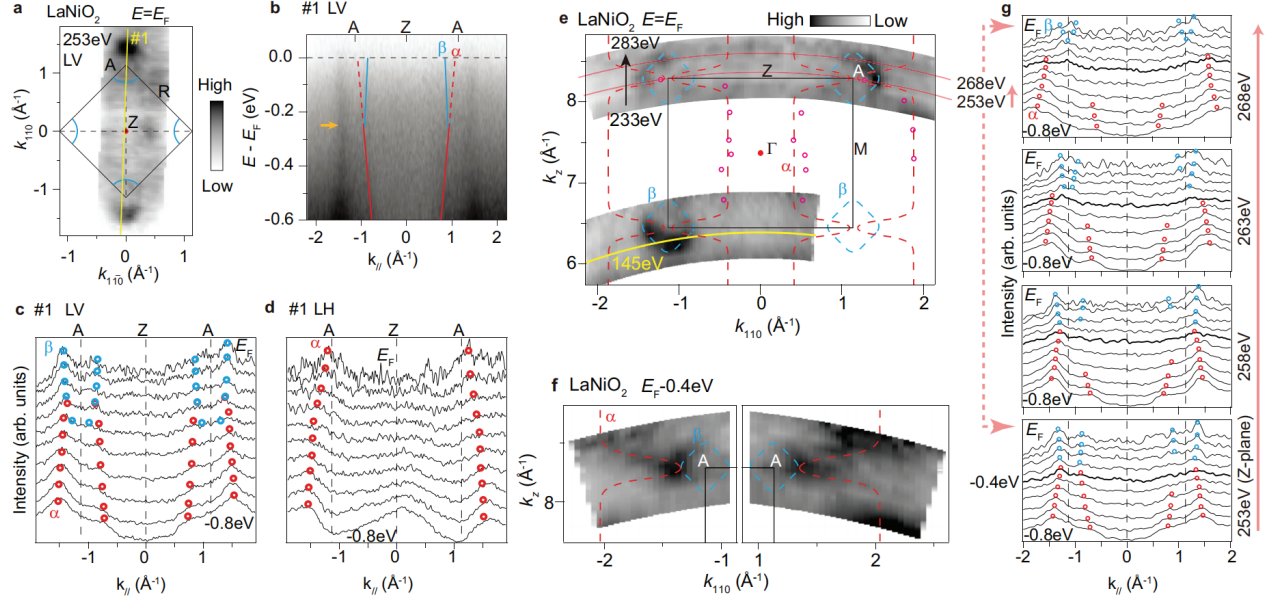


FIG. 4: Three-dimensional structure of the Fermi surface. **a**, In-plane photoemission intensity map of 1.2 uc-BTO/21 uc-LaNiO₂/SrTiO₃ at the Z-A-R plane measured by 253 eV photons with linear vertical (LV) polarization. The integration is over the energy window of $E_F \pm 0.2$ eV. The electron pockets of β band are illustrated by blue curves. **b**, Photoemission intensity along A-Z-A (the cut #1 in panel **a**). The hole-like dispersion of α (red lines) crosses with the electron-like dispersion of β . The orange arrow points out the crossing point. **c, d**, MDCs along cut #1 taken by LV (**c**) and LH (**d**) polarizations, respectively. The circle markers track the local maxima/shoulders to show the dispersion of α (red circles) and β (blue circles) bands. **e**, k_z dependent photoemission map integrated over $E_F \pm 0.2$ eV in the Γ -M-A-Z plane, measured on 1.2uc-BTO/21uc-LaNiO₂/SrTiO₃ taken with 233~283 eV photons in LV polarization, and measured on 21uc-LaNiO₂/SrTiO₃ taken with 130~170 eV photons with mixed polarization. The red circle markers track the local maximal photoemission intensity of LH polarization, which is supported by MDCs in Fig. S10. **f**, k_z dependent photoemission intensity map of 1.2uc-BTO/21uc-LaNiO₂/SrTiO₃ in the Γ -M-A-Z plane, taken with 233~283 eV photons in LV polarization, integrated over $[E_F - 0.5$ eV, $E_F - 0.3$ eV]. According to the experimental data points (see MDCs in Supplementary Fig.S10), the red dashed curves and blue dashed curves illustrate the iso-energy contour of α and β bands, respectively. **g**, MDCs showing the evolution of dispersive bands when the photon energy changes from 253 eV (Z-plane) to 268 eV, whose momentum range is indicated in panel **e**.

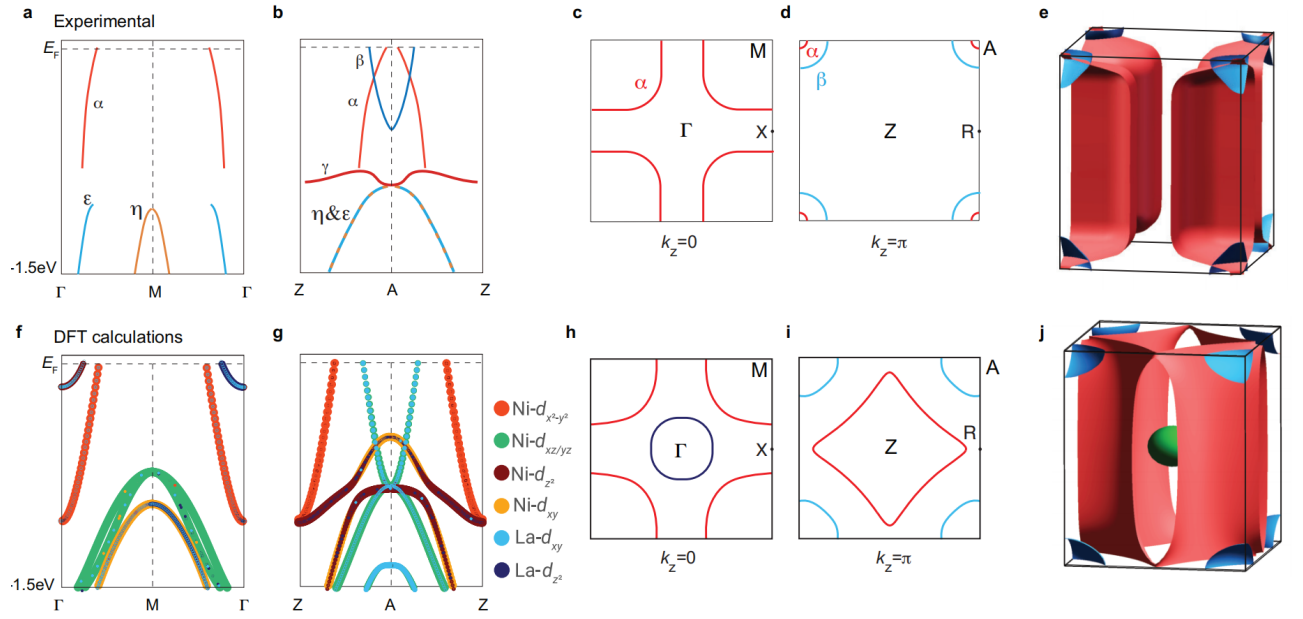


FIG. 5: **Comparison between experimental electronic structures and DFT calculations of LaNiO₂.** **a, b**, Summary of experimental electronic band dispersions along Γ -M (**a**) and Z-A (**b**). **c, d**, Illustration of Fermi surfaces in the Γ -X-M (**c**) and Z-A-R (**d**) planes determined by experimental data. **e**, Three-dimensional illustration of the Fermi surface determined by experimental data. **f, g**, the calculated band structure by DFT along Γ -M (**f**) and Z-A (**g**). The bands are color-coded based on their orbital character. **h, i**, Calculated Fermi surfaces in the Γ -X-M (**h**) and Z-A-R (**i**) planes. **j**, Calculated Fermi surfaces in the three-dimensional BZ.